Taylor & Francis
Taylor & Francis Group

RESEARCH ARTICLE

OPEN ACCESS Check for updates

Alginate-based aerogels as wound dressings for efficient bacterial capture and enhanced antibacterial photodynamic therapy

Ning Guo[a]*, Yu Xia[a]*, Weishen Zeng[a], Jia Chen[a], Quanxin Wu[a], Yaxin Shi[a], Guoying Li[a], Zhuoyi Huang[a], Guanhai Wang[a] and Yun Liu[a,b]

[a]Guangdong Key Laboratory for Research and Development of Natural Drugs, School of Pharmacy, Guangdong Medical University, Zhanjiang, China; [b]The Marine Biomedical Research Institute of Guangdong, Zhanjiang, China

ABSTRACT

The development of novel wound dressings, such as aerogels, with rapid hemostasis and bactericidal capacities for pre-hospital care is necessary. To prevent the occurrence of bacterial resistance, antibacterial photodynamic therapy (aPDT) with broad-spectrum antibacterial ability and negligible bacterial resistance has been intensively studied. However, photosensitizers often suffer from poor water solubility, short singlet oxygen ($^1O_2$) half-life and restricted $^1O_2$ diffusion distance. Herein, sodium alginate was covalently modified by photosensitizers and phenylboronic acid, and cross-linked by Ca(II) ions to generate SA@TPAPP@PBA aerogel after lyophilization as an antibacterial photodynamic wound dressing. Afterwards, its photodynamic and bacterial capture activities were intensively evaluated. Furthermore, its hemostasis and bactericidal efficiency against *Staphylococcus aureus* were assessed via *in vitro* and *in vivo* assays. First, chemical immobilization of photosensitizers led to an enhancement of its solubility. Moreover, it showed an excellent hemostasis capacity. Due to the formation of reversible covalent bonds between phenylboronic acid and diol groups on bacterial cell surface, the aerogel could capture *S. aureus* tightly and dramatically enhance aPDT. To sum up, the prepared aerogel illustrated excellent hemostasis capacity and antibacterial ability against *S. aureus*. Therefore, they have great potential to be utilized as wound dressing in clinical trials.

1. Introduction

As the largest organ of human body, the skin plays essential roles in defending against bacterial pathogens and environmental assaults (McGrath & Uitto, 2008; Meglio et al., 2011; Lai-Cheong & McGrath, 2021). However, skin trauma often occurred with injuries, such as cuts, contusions, military casualties, traffic accidents, and surgeries. Unfortunately, serious skin damage could lead to excessive blood bleeding and pathogenic infection. As reported, un-controlled hemorrhage has become the main cause of trauma death worldwide (Gaston et al., 2018). On the occasion of skin damage, wound dressings are employed as pre-hospital care by covering the wound area to stop bleeding and protect the wound site from early contamination of bacterial adhesion and settlement. Although various materials are commonly applied in clinical trials (Xian et al., 2020; Dong & Guo, 2021), there is still an increasing demand for the exploitation of novel functional materials with rapid hemostasis and antibacterial ability for trauma emergency treatment and temporary protection.

Despite diverse materials used in wound dressings (Maleki et al., 2021; Liang et al., 2022), aerogels have been emergingly studied and demonstrated promising application prospect in hemostasis (Li et al., 2020a,b; Yao et al., 2022; Zheng et al., 2022). According to IUPAC (international union of pure and applied chemistry), aerogels are defined as gels comprised of microporous solid in which dispersed phase is gas. In another word, aerogels are a type of ultra-light materials with high porosity and large surface area. Actually, fluid absorption capacity is essential in the prevention of bleeding due to the huge amount of blood exudate (Yao et al., 2021). Owning to the high porosity of aerogels, the wound dressings are endowed with excellent blood exudate absorption ability. Compared to traditional wound dressings, aerogels-based wound dressings not only have blood exudate absorption ability but also possess a key capacity in maintaining the gaseous exchanges, which is also of importance for wound healing. In comparison with hydrogels, the highly porous network, adjustable surface properties, tunable pore sizes, low density and good biocompatibility of aerogels make them promising candidates for bactericidal applications

(Zhang et al., 2020). Aerogels can achieve rapid capture and efficient elimination of bacteria to effectively treat bacterial wound infections due to its high porosity and large surface area (Kaya et al., 2021). Considering that ideal aerogels should be nontoxic, biocompatible and biodegradable, alginate is a good option and has been intensively researched for the fabrication of aerogels. As an anionic polysaccharide biopolymer isolated from brown algae, alginate illustrates negligible toxicity, low immunogenicity, excellent biocompatibility and biodegradability, which make it suitable for *in vivo* applications (Aderibigbe & Buyana, 2018; Ren et al., 2018; Varaprasad et al., 2020). Due to its gelling ability via Ca(II)-mediated ionotropic gelation under mild conditions, alginate allows the formation of hydrogels. Eventually, freeze-drying technology offers a green method for preparing alginate-based aerogels from wet gels to preserve the cross-linked 3D structures. Besides, the obtained aerogels achieve the continuous release of Ca(II) as a blood coagulation factor to accelerate hemostasis (Stenflo et al., 2000; Toyoda et al., 2018).

To further avoid bacterial infection, bactericidal ability is essential for wound dressings. Accordingly, antibiotics are preferentially used to strengthen their antibacterial effect. Regrettably, long term and abuse of antibiotics lead to the occurrence of bacterial resistance (Auzin et al., 2021; Lai et al., 2021; Bassetti et al., 2022). As predicted by World Health Organization (WHO), it could cause the death of nearly 10 million people each year by 2050. To avert the use of antibiotics and prevent the occurrence of bacterial resistance, novel antibiotic-free treatments have been emergingly developed (Yu et al., 2018; Guo et al., 2020; Wu et al., 2021), for instance, antibacterial photodynamic therapy (aPDT). aPDT takes full advantage of singlet oxygen ($^1O_2$) generated by photosensitizers for effective bacterial inactivation. During the process, irreparable oxidative damage is caused by $^1O_2$ to vital cellular components, such as lipids, proteins and DNA, which leads to the death of bacteria with negligible bacterial resistance. Due to its broad-spectrum antibacterial capacity and remote controllability, intensive research attentions have been continuously devoted to aPDT in the past decades (Jia et al., 2017; Sun et al., 2019; Dharmaratne et al., 2020; Li et al., 2020; Xiao et al., 2020; Feng et al., 2021). Fortunately, aPDT in wound dressing platforms does not have the two main drawbacks: inadequate oxygen supply and limited penetration depth of laser light. However, further application of aPDT is still severely limited by its unsatisfactory therapeutic efficiency caused by short lifetime and restricted diffusion distance of $^1O_2$ (Diniz et al., 2015). To further improve the therapeutic efficiency of aPDT in wound dressings, novel approaches are urgently needed to address these issues.

Recently, the boronic acid, especially phenylboronic acid, has been widely used in antibacterial applications due to its capacity to form reversible covalent bonds with diols (Cheng et al., 2020; Hu et al., 2020). In another word, it could bind to any diol containing compounds to form boronic esters. Consequently, the binding of boronic acid to diol containing antibacterial agents is responsive to acidic pH, which has been utilized for infectious microenvironment-responsive bactericidal release during treatments (van der Vlies et al., 2019; Zhao et al., 2021; Zheng et al., 2021). More importantly, boronic acid is also employed as a functional group for specifically reacting with the diol groups of glycoproteins and polysaccharides on the bacterial cell walls to achieve bacterial targeting attachment and amplify their accumulation on the cell walls (Beyranvand et al., 2020; Wang et al., 2021). Therefore, boronic acid surface modification is a promising strategy for improved therapeutic efficiency during anti-infective therapy.

Herein, sodium alginate (SA)-based functional molecule, SA@TPAPP@PBA, has been rationally designed and successfully prepared by chemically modifying SA with 3-aminophenylboronic acid (PBA) and photosensitizer molecules (tetra(4-aminophenyl)porphyrin, TPAPP, Scheme 1). Through
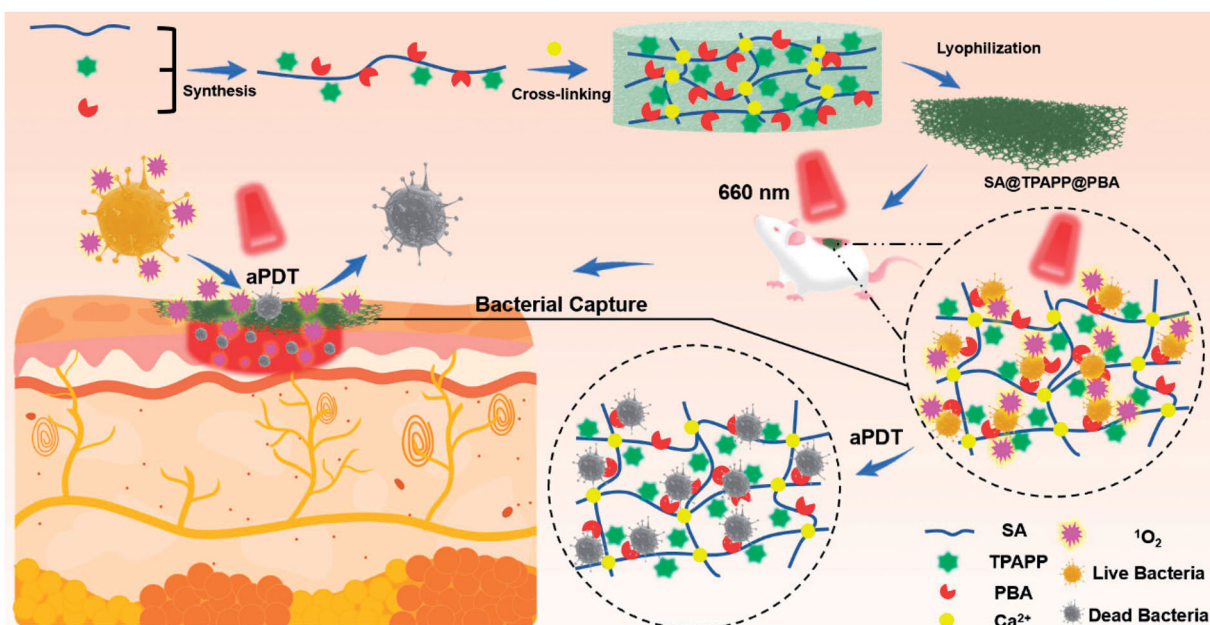
Scheme 1. Schematic illustration of alginate-based aerogel and its application as antibacterial photodynamic wound dressing.

cross-linking with Ca(II) ions, SA@TPAPP@PBA aerogel could be generated after lyophilization as a novel aPDT wound dressing. Due to its high porosity, SA@TPAPP@PBA aerogel could efficiently absorb blood exudate and turn into hydrogel to stop bleeding and inhibit the formation of bacterial-growth-promoting exudate-filled areas. Besides, the chemical immobilization of TPAPP led to an increment of its water solubility and biocompatibility. Owning to the formation of reversible covalent bonds between PBA and the diol groups of glycoproteins on the bacterial cell surface (Halbus et al., 2019; Wang et al., 2020), SA@TPAPP@PBA aerogel could capture *Staphylococcus aureus* (*S. aureus*) tightly. More importantly, the efficient bacterial capture dramatically contributed to the achievement of enhanced aPDT upon 660 nm laser irradiation. *In vitro* and *in vivo* assays illustrated that SA@TPAPP@PBA aerogel could fulfill the demand of stopping bleeding and avoiding bacterial infection synchronously, which should be taken into consideration for anti-infective therapy in future.

2. Materials and methods

2.1. Materials

5,10,15,20-Tetra (4-aminophenyl) porphyrin (TPAPP) was purchased from Zhengzhou Anmusi Chemical Products Co., Ltd. (Zhengzhou, China). Sodium alginate (SA), 3-aminophenylboronic acid, *N*-(3-dimethylaminopropyl)-N'-ethylcarbodiimide hydrochloride (EDC·HCl), and CaCl$_2$ were purchased from Shanghai Aladdin Biochemical Technology Co., Ltd. (Beijing, China). N-Hydroxysuccinimide (NHS) was purchased from Tianjin C&S Biochemical Technology Co., Ltd. (Shanghai, China). 1,3-Diphenylisobenzofuran (DPBF, 97%) was purchased from Acros Organics (Geel, Belgium). Luria–Bertani (LB) Broth powder was purchased from Beijing Solarbio Biotechnology Co., Ltd. (Beijing, China). Mueller Hinton agar medium was purchased from Guangdong Huankai Microbial Technology Co., Ltd. (Guangdong, China). Dulbecco's modified Eagle's medium (DMEM) and fetal bovine serum (FBS) were purchased from Gibco (Carlsbad, CA, USA). SYTO 9 and propidium iodide (PI) were purchased from Sigma Co, Ltd. (St. Louis, MO, USA). All solvents and reagents were of analytical grade and used as received unless declared.

2.2. Cell lines and cell culture

The mouse fibroblast cells (L929) were obtained from Guangzhou Medical University (Guangdong, China). L929 cells were cultured in DMEM medium, supplemented with 10% FBS and 1% penicillin–streptomycin at 37 °C under a humid atmosphere containing 5% CO$_2$.

2.3. Synthesis of SA@TPAPP@PBA molecules

SA (198.0 mg) was dissolved in 50 mL DI water, EDC·HCl (193.5 mg) and NHS (117.1 mg) were added to activate the carboxyl groups for 45 min. Then TPAPP (5 mg) in ethanol (50 mL) was added slowly and stirred for 24 h (Scheme 2).

After dialysis against water/ethanol solvent mixtures (10:1, *v/v*) for 2 d, SA@TPAPP was obtained via lyophilization. Next, PBA (136.9 mg) was coupled to SA@TPAPP with EDC·HCl and NHS by using ethanol/water mixtures (1:1 *v/v*) as co-solvent. After dialysis for 2 d, SA@TPAPP@PBA molecules were obtained via lyophilization.

2.4. Preparation of SA@TPAPP@PBA aerogel

The aqueous solutions of SA, SA@TPAPP or SA@TPAPP@PBA (2%) were poured into the molds and kept in fridge at 4 °C to eliminate bubbles. And the porous skeletons were obtained by lyophilization. Finally, the skeletons were cross-linked by CaCl$_2$ aqueous solution (500 mM) and lyophilized to obtain the corresponding aerogels.

2.5. Characterization

The UV–vis absorption spectra was recorded on UV-visible spectrophotometer (UV-6000PC, Shanghai Metash Instruments Co., Ltd, Shanghai, China). Fourier transform infrared (FTIR) spectra were tested from 400 to 4000 cm^{-1} using a FTIR spectrometer (WQF-510A, Beijing Rayleigh Analytical Instrument Co. Ltd, Beijing, China). The morphology and structure of the aerogels were observed by scanning electron microscope (SEM, JSM-IT500, JEOL, Tokyo, Japan). Confocal laser scanning fluorescence microscope (CLSM) images of bacteria were taken by using an oil immersed 63 × objective lens (Leica, SP8, Mannheim, Germany).

2.6. Water absorption ability (W$_{AA}$)

Firstly, the weight (W$_0$) of the aerogels (Φ 8 × 2 mm) was recorded including SA, SA@TPAPP, and SA@TPAPP@PBA aerogels. Then all the aerogels were entirely immersed into DI water at 37 °C for 30 min until reaching saturation. After removing the surface moisture, the saturated weight (W$_1$) of the aerogels was recorded. W$_{AA}$ can be calculated according to the following formula:

$$W_{AA}(\%) = (W_1 - W_0)/W_0 \times 100\% \qquad (1)$$

2.7. Porosity (P) of aerogels

First, the weight (W$_0$) and volume (V) of the aerogels were recorded, including SA, SA@TPAPP, and SA@TPAPP@PBA aerogels. Then all the aerogels were entirely immersed into ethanol and the air was fully removed by vacuum. After 30 min, the weight of the aerogels (W$_f$) was recorded. P can be calculated according to the following formula:

$$P = (W_f - W_0)/\rho_{EtOH} \cdot V \times 100\% \qquad (2)$$
$$\left(\rho_{EtOH} = 0.78935g \ cm^{-3}\right)$$

2.8. $^1O_2$-generation ability evaluation

DPBF was used as a probe to detect the production of $^1O_2$. The aerogels, including SA, SA@TPAPP, and SA@TPAPP@PBA aerogels, were put into the bottom of cuvette, respectively.
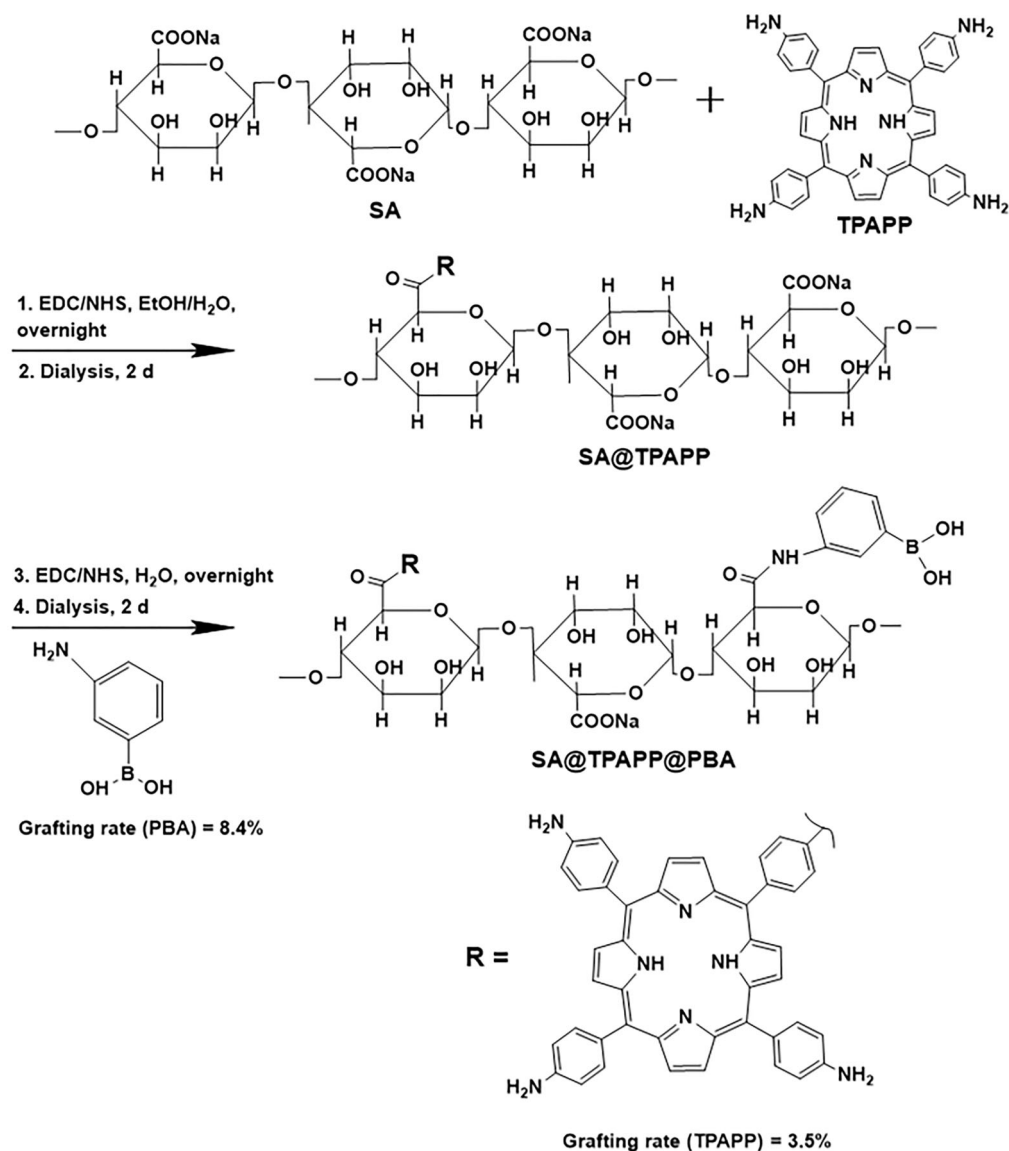
Scheme 2. Synthesis of SA@TPAPP and SA@TPAPP@PBA molecules.

After the addition of DPBF solution of acetonitrile (0.04 mM, 2 mL), the mixtures were irradiated with a 660-nm laser light at 50 mW cm^{-2} for 7 min. The absorption spectrum of the samples was recorded every minute by UV–vis spectrophotometer. As a contrast, the non-photodynamic samples were also recorded.

2.9. Bacteria culture

Staphylococcus aureus (S. aureus, ATCC 25923) was kindly provided by Guangzhou Institute of Microbiology. The single colony of bacteria was suspended in LB medium and then incubated overnight at 37 °C under 220 rpm shaking. After centrifugation, logarithmic growth bacteria were obtained and re-suspended in fresh LB medium.

2.10. Bacterial capture assays

Bacterial adhesion on SA, SA@TPAPP and SA@TPAPP@PBA aerogels was assessed by culturing S. aureus suspension (10^7

CFU mL^{-1}) with the aerogels. Briefly, the aerogels were immersed into the bacterial suspension (1 mL) for 3 h at 37 °C. Then non-immobilized bacteria were washed away with 0.9% NaCl. After fixation of the immobilized bacteria with glutaraldehyde solution (2.5%) for 12 h, they were dehydrated in series of ethanol solutions (30, 50, 70, 80, 90, and 100%) for 10 min and lyophilized. Finally, the samples were sputtered with platinum and observed by SEM.

2.11. In vitro antibacterial assays

In vitro antibacterial activities of the aerogels were evaluated by using S. aureus as model bacteria. All devices and aerogels were treated by an ultraviolet lamp for 30 min in advance. Firstly, the aerogels were put into the bottom of 48 well plates, respectively. After the addition of bacterial suspension (10^7 CFU mL^{-1}, 500 μL) to each well and incubation in dark for 3 h, the aerogels were equally divided into two groups for light free and light treatment with a 660 nm laser

light (50 mW cm^{-2}, 60 min), separately. Finally, the antibacterial properties of the aerogels were tested by the agar plate counting. Through the incubation of plates at 37 °C for 12 h, the antibacterial rate of aerogels can be calculated by counting the number of colonies according to the following equation:

$$\text{Antibacterial rate } (\%) = (N_C - N_S)/N_C \times 100\% \qquad (3)$$

where N_C is the number of colonies incubated with DI water, and N_S stands for the number of colonies incubated with the aerogels.

2.12. Fluorescence microscopic observation (live/dead)

Bacteria dispersion (10^7 CFU mL^{-1}, 500 μL) was incubated with aerogels at 37 °C for 3 h. Then they were equally divided into two groups for light free and light treatment with a 660 nm laser light (50 mW cm^{-2}, 60 min), separately. Afterwards, the mixture was centrifuged at 5000 rpm for 5 min to remove the supernatant and washed with PBS twice. The aqueous solution of 0.6 μL SYTO 9 and 10 μL PI in 990 μL PBS was prepared, and 300 μL of the solution was mixed with the obtained bacterial pellet in dark for 20 min at 37 °C. In this way, the live and dead bacteria were stained for green color by SYTO 9, and the dead bacteria were stained for red color by PI. All samples were fixed on confocal small dish with 2.5% glutaraldehyde solution, and the images were captured CLSM.

2.13. Hemolysis assays

Fresh blood of SD rats (1 mL) was suspended in PBS (10 mL, pH 7.4, 10 mM with 0.9% NaCl) and centrifuged at 1000 rpm for 10 min. The supernatant was thrown away to collect red blood cells (RBCs). The collected RBCs were rinsed with huge amount of PBS until the supernatant was colorless. Finally, the RBCs were diluted with PBS into 4% (volume concentration).

First, the aerogels were grinded into powder for further use. The aqueous suspension of powders (2 mg mL^{-1}, 0.5 mL) was mixed with RBCs suspension, and the mixture was incubated at 37 °C for 2 h. After centrifugation at 1000 rpm for 5 min, the supernatant was collected and kept at room temperature for 30 min to fully oxidize the hemoglobin to form oxyhemoglobin. RBCs treated with deionized water were used as the positive control group, and RBCs treated with 0.9% NaCl were used as the negative control group. Finally, the absorbance at 540 nm was recorded by a microplate reader to calculate hemolysis rate (HR) according to the following formula:

$$\text{HR } (\%) = (A_s - A_n)/(A_p - A_n) \times 100\% \qquad (4)$$

where A_s is the absorbance of RBCs incubated with aerogels, A_n reflects the absorbance of RBCs incubated with 0.9% NaCl, and A_p stands for the absorbance of RBCs incubated with DI water.

2.14. Cytotoxicity assay

The toxicity of the aerogels in L929 was assessed by MTT assay and Live/Dead assays. L929 cells were seeded in a 48 well plate with a density of 6000 cells per well, and incubated at 37 °C for 24 h to achieve adherent growth. After replacing the supernatant with fresh DMEM medium, the aerogels (SA, SA@TPAPP, SA@TPAPP@PBA, 1 mg mL^{-1}) were incubated at 37 °C for 24 h. Then 10 μL of MTT (5 mg mL^{-1}) was added into each well for another 4 h and rinsed with PBS. In order to dissolve the produced formazan crystals, DMSO (100 μL) was added. Finally, the absorbance of obtained mixture at 570 nm was recorded with a microplate reader.

Besides, Live/Dead assays was conducted with L929 cells in a 6-well plate with a density of 2×10^5 cells per well and incubated at 37 °C for 24 h. After sucking up the supernatant, the suspension of the powder (SA, SA@TPAPP, SA@TPAPP@PBA, 1 mg mL^{-1}, 1 mL) were added and incubated at 37 °C for 24 h. Then 500 μL of calcein-AM/propidium iodide dye was added to stain the cells for 15 min after washing 3 times. And the fluorescence was observed by the inverted fluorescence microscope (Zeiss, Axio Observe 7).

2.15. Hemostatic experiments

The hemostatic capacities of the aerogels were tested by the rat-tail cutting experiment. All animal studies described were approved by the animal center of Guangdong Medical University. Twelve SD rats used in this experiment were randomly divided into four groups. 30% length of their tails were cut and quickly wrapped with four different samples, including gauze, SA, SA@TPAPP, and SA@TPAPP@PBA aerogels, respectively. Then the hemostatic capacities of the individual samples were evaluated by comparing their weight and time of blood loss afterwards.

2.16. Blood cell adhesion test

The adhesion of blood cells on the aerogels was evaluated by dropping the whole blood onto the gauze and the aerogels (SA, SA@TPAPP, and SA@TPAPP@PBA), respectively, and incubated for 5 min at 37 °C. After rinsing the unimmobilized blood cells away, 2.5% glutaraldehyde was added to fix the blood cells for 3 h. After that the aerogels were dehydrated steadily by employing ethanol-aqueous solutions (50, 60, 70, 80, 90, and 100%). Finally, the morphology of the obtained samples was visualized by SEM.

2.17. The blood-clotting index (BCI)

All the aerogels (SA, SA@TPAPP, and SA@TPAPP@PBA) were cut into the cylindrical specimens with the same size (diameter: 8 mm, height: 5 mm). After that the recalcified blood aqueous solution (10 mM CaCl$_2$, 100 μL) was added onto the surfaces of the aerogels. After incubating at 37 °C for 2.5 min, huge amount of DI water (10 mL) was used to rinse the unattached blood away without destroying the clot. And the

absorbance of the supernatant at 540 nm (I_s) was recorded with the microplate reader. The positive control group (I_p) was recorded by directly mixing the bloods (100 μL) with DI water (10 mL). The BCI was calculated according to the following formula:

$$BCI (\%) = (I_s/I_p) \times 100\% \qquad (5)$$

2.18. In vivo antibacterial experiments

All animal experiments have received the animal ethical and welfare permission from the animal center of Guangdong Medical University (Dongguan, China). Male Sprague–Dawley (SD) rats (180–200 g) were purchased from Guangdong Provincial Animal Center (Guangzhou, China) and kept in the SPF animal house. The 24 SD rats used were randomly divided into eight groups (0.9% NaCl, SA, SA@TPAPP, SA@TPAPP@PBA, 0.9% NaCl + Light, SA + Light, SA@TPAPP + Light, SA@TPAPP@PBA + Light). The infectious model was built on the back skin of SD rats by punching a hole with a diameter of 8 mm. Staphylococcus aureus solution (10^9 CFU mL^{-1}, 10 μL) was dropped onto the wound site for 30 min. Then the aerogels were put onto the wound site, separately. The groups of light treatment were irradiated with a 660 nm laser light (50 mW cm^{-2}, 60 min). During the experiment, the wound area of the mice was photographed at 0, 7th, and 15th day. And all the mice were sacrificed at the 15th day. Finally, the skin tissues of the wound site were collected and fixed with paraformaldehyde (4%) for hematoxylin and eosin (H&E) staining.

2.19. Statistical analysis

The values were manifested as the mean ± standard deviation (SD), and the data were gathered based on more than three parallel experiments. The statistical analysis was concluded by using Student's t-test. In all test, the statistical significance for the test was set at $*p < .05$, $**p < .01$, and $***p < .001$.

3. Results and discussion

3.1. Preparation and characterization of SA@TPAPP@PBA aerogel

To confirm whether TPAPP and PBA were successfully immobilized to SA, the produced SA@TPAPP@PBA was characterized by FT-IR and UV-vis spectroscopy. As shown in Figure 1, the absorption intensity at 1610 cm^{-1} (amide I band) in SA@TPAPP and SA@TPAPP@PBA is comparatively enhanced than that in SA. Due to the potential interference of O–H bending vibration absorption peak in adsorbed water, UV–vis spectroscopy was employed to further prove the preparation of SA@TPAPP@PBA molecules. According to UV–vis analysis (Figure S1), the grafting rates of TPAPP and PBA were determined to be 3.5 and 8.4%, respectively.

As illustrated in Scheme 1, SA@TPAPP@PBA aerogel was fabricated by lyophilizing the Ca(II)-crosslinked SA@TPAPP@PBA hydrogel (Figure 2(a)). The water absorption
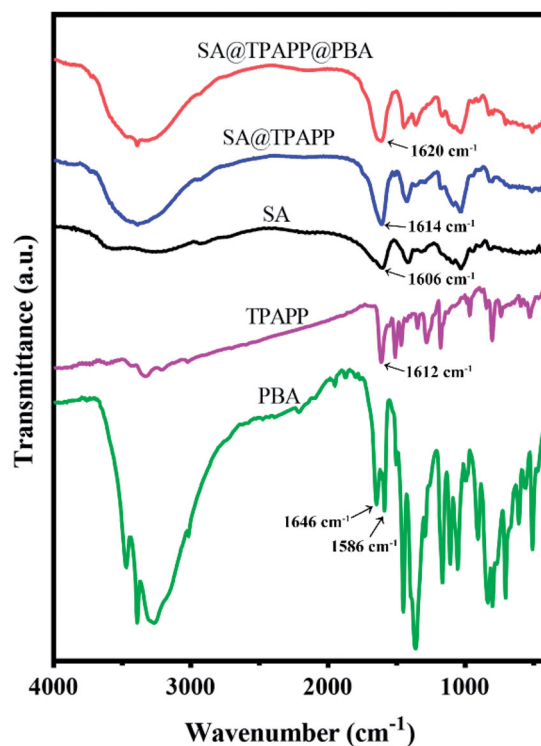

Figure 1. FTIR spectra of PBA, TPAPP, SA, SA@TPAPP, and SA@TPAPP@PBA.

ability and porosity of the aerogels were tested, respectively (Figure 2(b,c)). And the experimental results showed that SA@TPAPP@PBA aerogel achieved a high water absorption ability of 1199.1% and porosity of 79.4%, separately. Meanwhile, the morphology of aerogels was visualized by SEM (Figure 2(d)). Compared with gauze, lamellar and pore structures were formed in aerogels, which were crucial blood exudate absorption during hemostasis and bacterial capture. Thus, all prepared aerogels exhibited good water absorbing capacity.

Since high amount of $^1O_2$ was produced as bactericidal during aPDT at the wound site, DPBF assay was performed to evaluate the $^1O_2$ generating ability of SA@TPAPP@PBA aerogel (Figures 3 and S2). Due to the reaction ability of DPBF with $^1O_2$ to generate the non-absorbing o-dibenzoylbenzene, it was employed as a quencher. And the absorption at 410 nm was used to quantify the relative consumption of DPBF. Actually, the DPBF absorption intensity of SA@TPAPP@PBA aerogel dramatically decreased after the exposure to a 660 nm laser irradiation compared with control samples (Figure 3(a)). Besides, absolute $^1O_2$ formation could be readily controlled by the irradiation time (Figure 3(b)).

3.2. In vitro antibacterial activity

Due to the formation of boronic esters between boronic acid and various glycoproteins and polysaccharides on the surfaces of bacteria, boronic acid was widely used as an appropriate recognition or targeting molecule in bacteria detection and anti-infective therapy (Galstyan et al., 2017; Zheng et al., 2018; Halbus et al., 2019; Wang et al., 2020). In our research, PBA was employed in SA@TPAPP@PBA aerogel to recognize
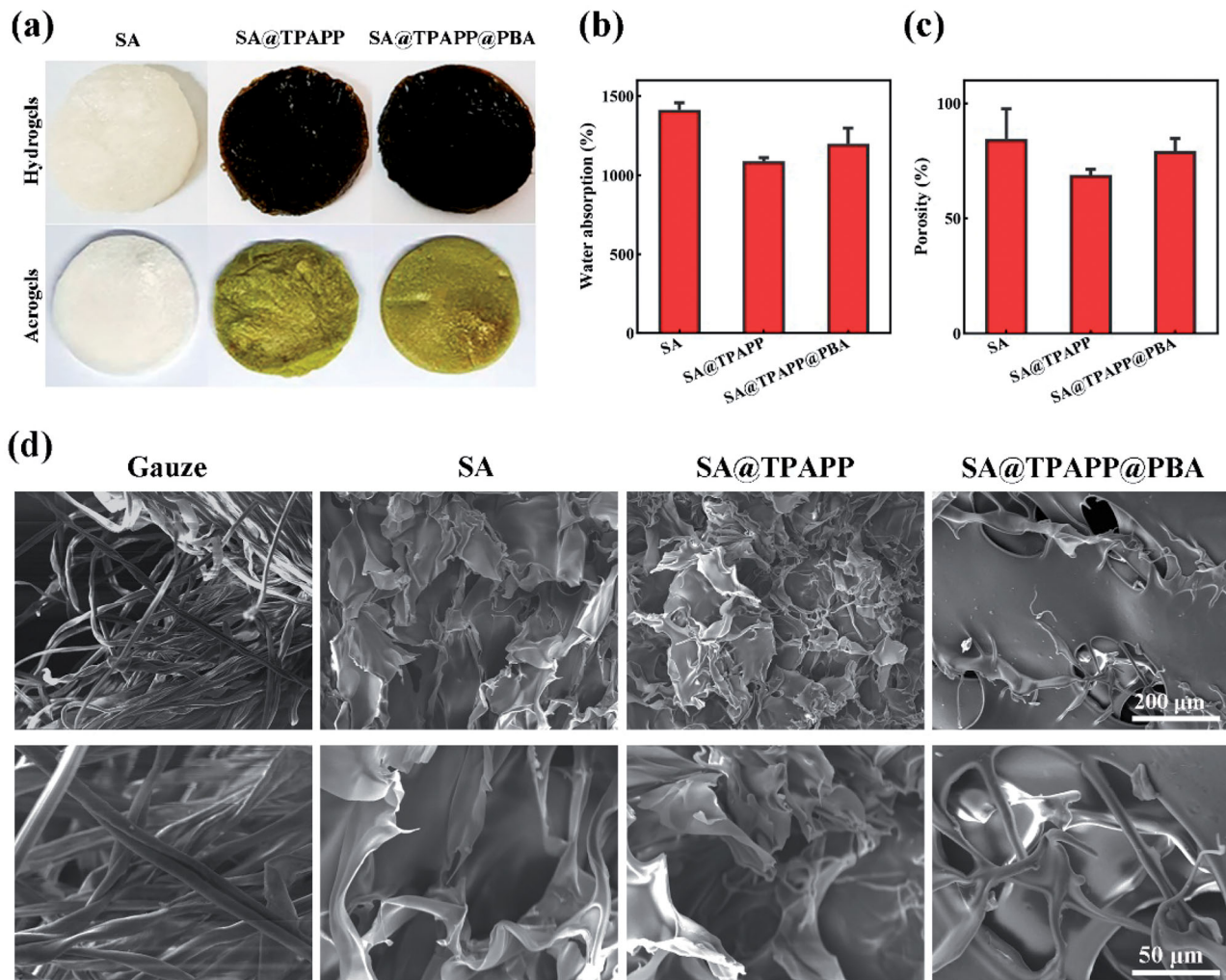
Figure 2. (a) The photographs of hydrogels and aerogels. (b) Water absorption rates and (c) porosity rates of SA, SA@TPAPP, and SA@TPAPP@PBA aerogels. (d) Morphology of gauze and aerogels. scale bar: 200 μm (top of the panel) and 50 μm (bottom of the panel).
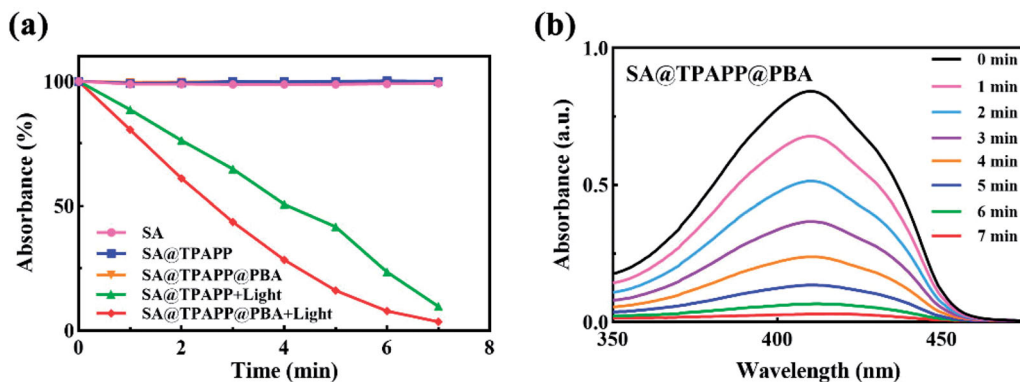

Figure 3. (a, b) UV–vis absorption spectra of DPBF treated with 660 nm laser light on/off. The curve of SA@TPAPP@PBA overlapped with that of SA and SA@TPAPP in (a).

and capture *S. aureus* through covalent diol-binding. Owning to shortened distance between bacteria and photosensitizer molecules/$^1O_2$, the therapeutic efficiency of aPDT could be greatly improved. To study the process of bacterial capture, *S. aureus* were incubated with the aerogels in dark. Afterwards, the obtained aerogels were observed by SEM. As shown in Figure 4(a,b), SA@TPAPP@PBA aerogel adsorbed more *S. aureus* than SA and SA@TPAPP aerogels, which was

attributed the targeting function of PBA. Predictably, this could lead to a more efficient deconstruction of cell membranes via generated $^1O_2$ and improved photodynamic inactivation of *S. aureus* in the presence of 660 nm laser irradiation.

As wound dressing is used directly on wound area, adequate aPDT activity against wound infection is necessary for SA@TPAPP@PBA aerogel. Accordingly, its antibacterial
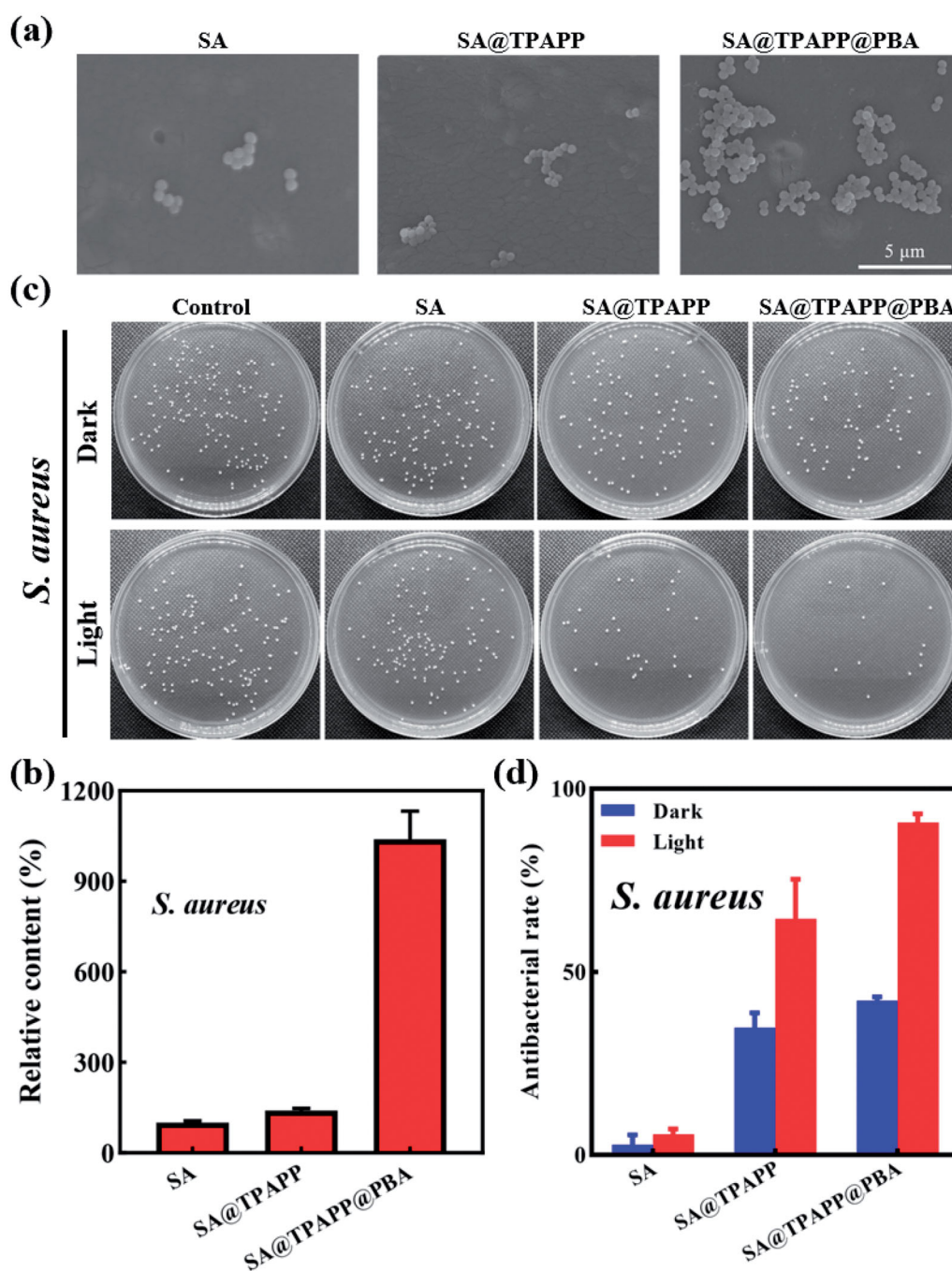
Figure 4. (a) SEM images of *S. aureus* adhesion on SA, SA@TPAPP, and SA@TPAPP@PBA aerogels. (b) Related histogram of *S. aureus* adhesion. (c) Photographs of bacterial colonies after different treatments. (d) The corresponding antibacterial rates determined by the plate counting method.

ability was evaluated by plate counting method against *S. aureus*. During the *in vitro* antibacterial assays, *S. aureus* were treated with SA, SA@TPAPP, and SA@TPAPP@PBA aerogels in the absence or presence of 660 nm laser irradiation (Figure 4(c,d)). The diminishment of viability in the presence of TPAPP without a 660 nm laser irradiation is regarded as dark toxicity. First, SA aerogel was co-cultured with *S. aureus* in the absence and presence of 660 nm laser irradiation, which showed no obvious difference in bacterial viability under the two conditions. Next, SA@TPAPP and SA@TPAPP@PBA aerogels were incubated with *S. aureus* in dark. As displayed in Figure 4(d), the outcomes exhibited a

slight antibacterial activity (<50%) against *S. aureus*, which might be attributed to the dark toxicity of TPAPP. Owning to the bacterial capture effect of PBA, SA@TPAPP@PBA aerogel possessed an improved antibacterial ability compared with SA@TPAPP aerogel. Finally, the therapeutic efficiency of aPDT was assessed by incubating SA@TPAPP and SA@TPAPP@PBA aerogel with *S. aureus* in the presence of 660 nm laser irradiation. As shown in Figure 4(d), SA@TPAPP aerogel reached an antibacterial rate of approximately 64.4%. Despite the fact that a restrained antibacterial activity was realized by SA@TPAPP aerogel, PBA modification was still necessary to achieve satisfactory aPDT efficiency. Actually, an enhanced
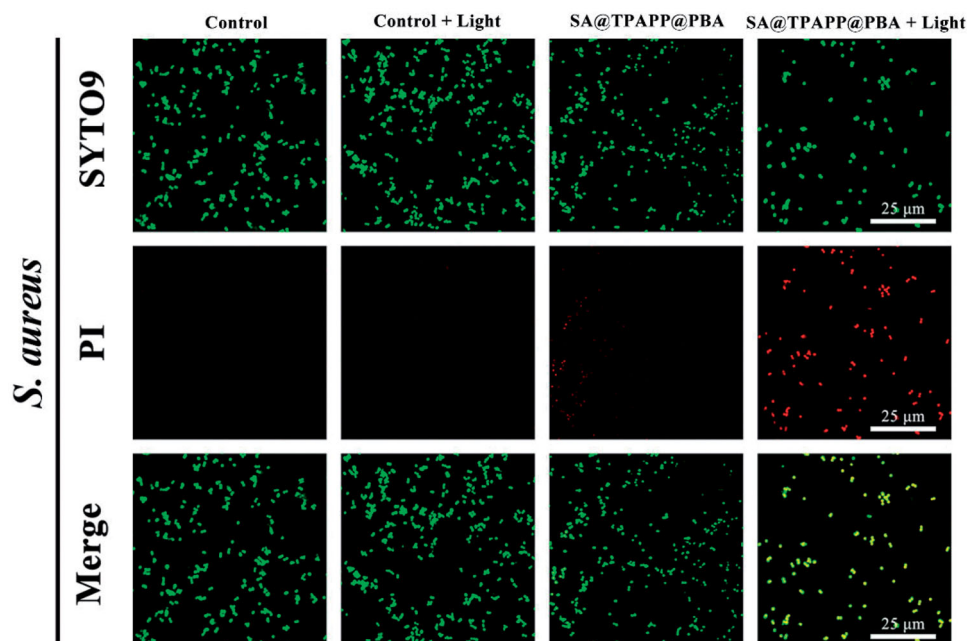
Figure 5. Confocal laser scanning microscopy (CLSM) images of *S. aureus* where dead/live bacteria are labeled green by SYTO 9 and dead bacteria are labeled red by PI (scale bar: 25 μm).

antibacterial effect was achieved by SA@TPAPP@PBA aerogels through PBA-mediated *S. aureus* capture function, which was 90.7%. Moreover, live/dead staining experiments were performed by employing SYTO-9 and PI staining kits. As illustrated in Figure 5, all control groups showed no obvious red fluorescence (dead bacteria). In contrast, an increased area of red fluorescence could be observed in groups of SA@TPAPP@PBA aerogel, which proved the augmented aPDT efficiency of SA@TPAPP@PBA aerogel. Meanwhile, SEM images of the bacteria before and after treatment in SA@TPAPP@PBA group were obtained (Figure S3). Massive wrinkles and dents were generated after light irradiation, which manifested its outstanding antibacterial ability via aPDT through the deconstruction of cell membrane. Therefore, all these results demonstrated the PBA enhanced aPDT efficiency of SA@TPAPP@PBA aerogel.

3.3. Biosafety of aerogels

Hemolysis, MTT assays, and live/dead cell staining were performed to assess the biocompatibility of SA@TPAPP@PBA aerogel (Figure 6). In the hemolytic test, freshly collected mouse red blood cells (RBCs) were utilized to co-culture with SA, SA@TPAPP, and SA@TPAPP@PBA aerogels at a high concentration (1 mg mL^{-1}), separately. H$_2$O and 0.9% NaCl were used as the positive and negative control, respectively. As can be seen from Figure 6(a), RBCs were totally ruptured and the supernatant was red in the positive control, while no obvious hemolytic effect could be observed both in the negative control and all other groups, including SA, SA@TPAPP and SA@TPAPP@PBA aerogels. Encouragingly, the hemolysis rate of SA@TPAPP@PBA aerogel (3.3%) was much less than the permissible limit (5%). L929 cells were selected in MTT and live/dead staining experiments to

evaluate the cell viabilities by incubating with SA, SA@TPAPP and SA@TPAPP@PBA aerogels at a high concentration (1 mg mL^{-1}), separately. Notably, all the three types of aerogels showed negligible cytotoxicity (Figure 6(b,c)). To sum up, the obtained experimental outcomes demonstrated the excellent biosafety of SA@TPAPP@PBA aerogel.

3.4. Hemostatic characterization

To avoid the excessive post-traumatic bleeding, hemostasis is an essential evaluation index for wound dressings. SD male rat was employed as animal model by cutting down part of its tail to evaluate the hemostatic property of SA@TPAPP@PBA aerogel (Figure 7(a)). Through the utilization of gauze, SA, SA@TPAPP, and SA@TPAPP@PBA aerogels, the blood loss and hemostatic time were recorded, respectively. As illustrated in Figure 7(b,c), the use of gauze led to a large amount of blood loss and copious blood flow for about 7 min. By using SA and SA@TPAPP aerogel, the blood loss and hemostatic time was dramatically diminished. Due to the excellent hemostatic property of SA@TPAPP@PBA aerogels, the blood loss and the hemostasis time were reduced by 77.5 and 60.6% compared to gauze.

In order to further investigate the hemostasis mechanism of SA@TPAPP@PBA aerogel, blood cell adhesion test was performed by dropping the whole blood onto gauze, SA, SA@TPAPP, and SA@TPAPP@PBA aerogels, respectively, and incubated for 5 min at 37 °C. After fixing with glutaraldehyde, the obtained samples were observed by SEM to visualize the adhesion geometry and morphology of RBCs, which were used to study the hemostatic mechanism (Figure 8(a)). Meanwhile, the amount of adhered blood cells was counted from SEM images to assess their hemostatic ability
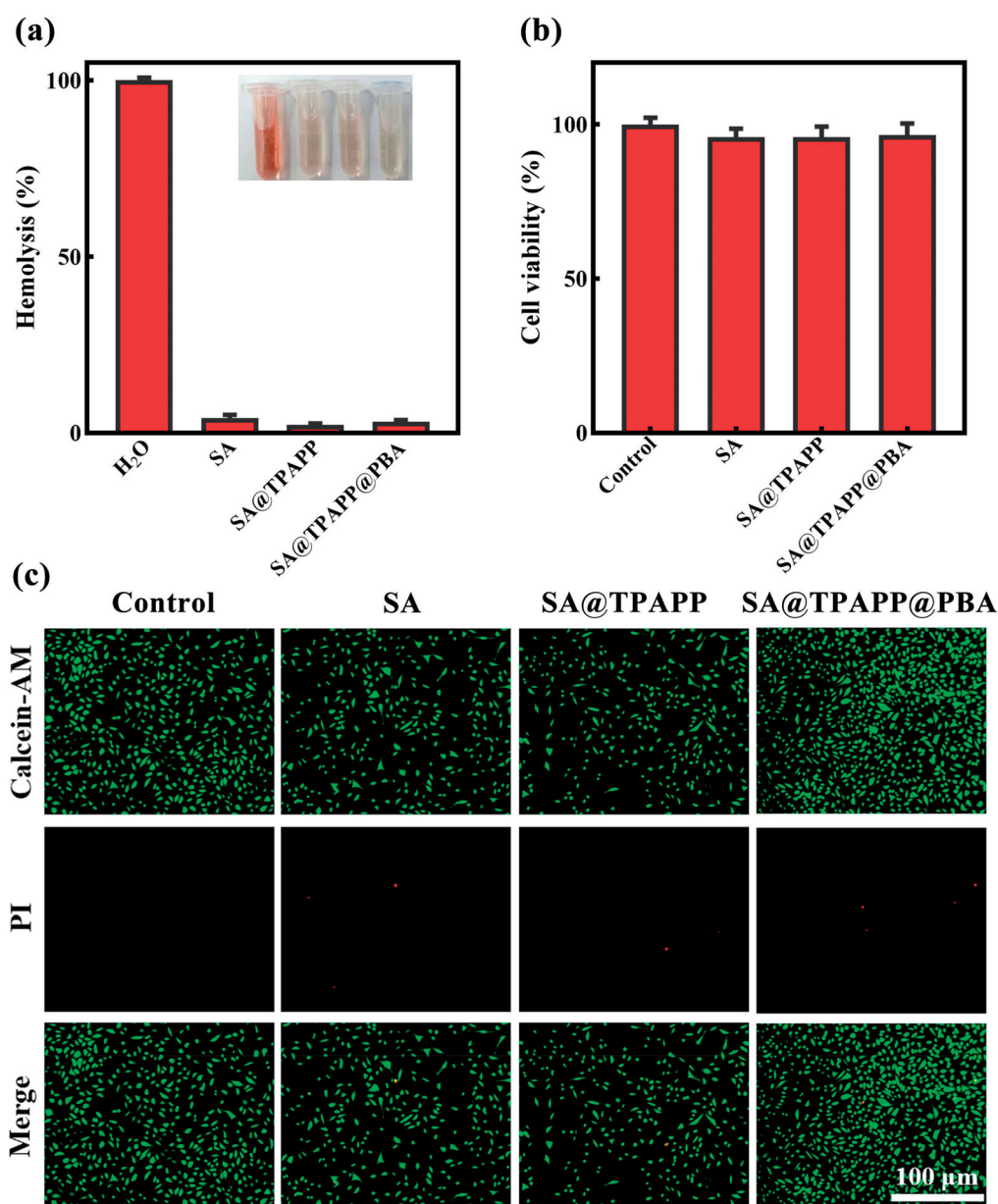
(a)

(b)

(c)

Figure 6. (a) Relative hemolysis ratio of SA, SA@TPAPP, and SA@TPAPP@PBA aerogels. Insets are the corresponding photographs. (b) Cell viability of L929 cells. (c) The images of live/dead staining of L929 cells. Scale bar: 100 μm.

(Figure 8(b)). As displayed in Figure 8(a,b), no obvious blood cell adhesion was observed on gauze. For SA aerogel, few blood cells (59.5×10^2 cell cm^{-2}) were adhered on the surface. In contrast, the number of adhered blood cells on SA@TPAPP aerogel (312.3×10^2 cell cm^{-2}) greatly increased compared to SA aerogel and gauze, owning to the positive charge of TPAPP. Notably, PBA led to approximately a three-fold increase in the number of adhered blood cells on SA@TPAPP@PBA aerogel with regular disk morphology compared to SA@TPAPP aerogel. Furthermore, values of blooding-clot index (BCI) were determined by dropping RBCs suspensions on gauze, SA, SA@TPAPP and SA@TPAPP@PBA aerogels and co-cultured at 37 °C for 2.5 min. As shown in Figure 8(c), SA@TPAPP@PBA aerogel possessed a much lower value of BCI (40.8%) than that of gauze (87.1%), indicating its effective blood-clotting ability. Thus, these results demonstrated that SA@TPAPP@PBA aerogel had extraordinary blood exudate absorption and blood clotting capacity to have potential applications in hemostasis as wound dressing.

3.5. In vivo antibacterial assays

Inspired by the excellent antibacterial ability, hemostatic capability and biocompatibility of SA@TPAPP@PBA aerogel in vitro, S. aureus-infected trauma model on the back skin of SD mice was employed to evaluate their in vivo therapeutic efficiency. After infecting for 30 min, the infected SD mice were divided randomly into eight groups: (1) Control, (2) SA, (3) SA@TPAPP, (4) SA@TPAPP@PBA, (5) Control + Light, (6) SA + Light, (7) SA@TPAPP + Light, and
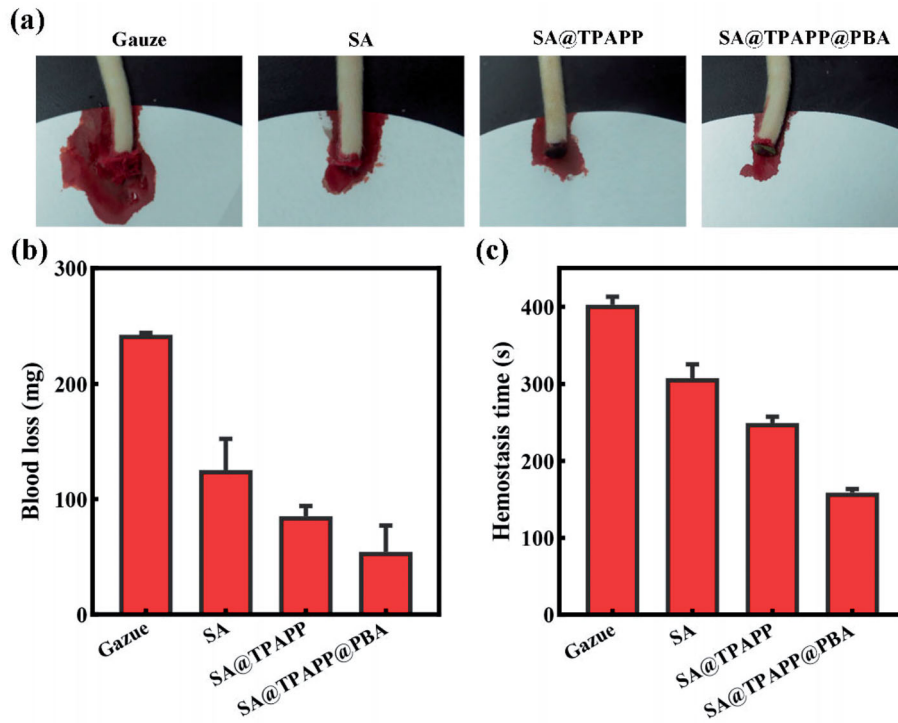
Figure 7. (a) Photographs of the hemostasis by using gauze, SA, SA@TPAPP, and SA@TPAPP@PBA aerogels. (b) Blood loss and (c) hemostatic time on the truncated rat-tail model by using gauze, SA, SA@TPAPP, and SA@TPAPP@PBA aerogels.
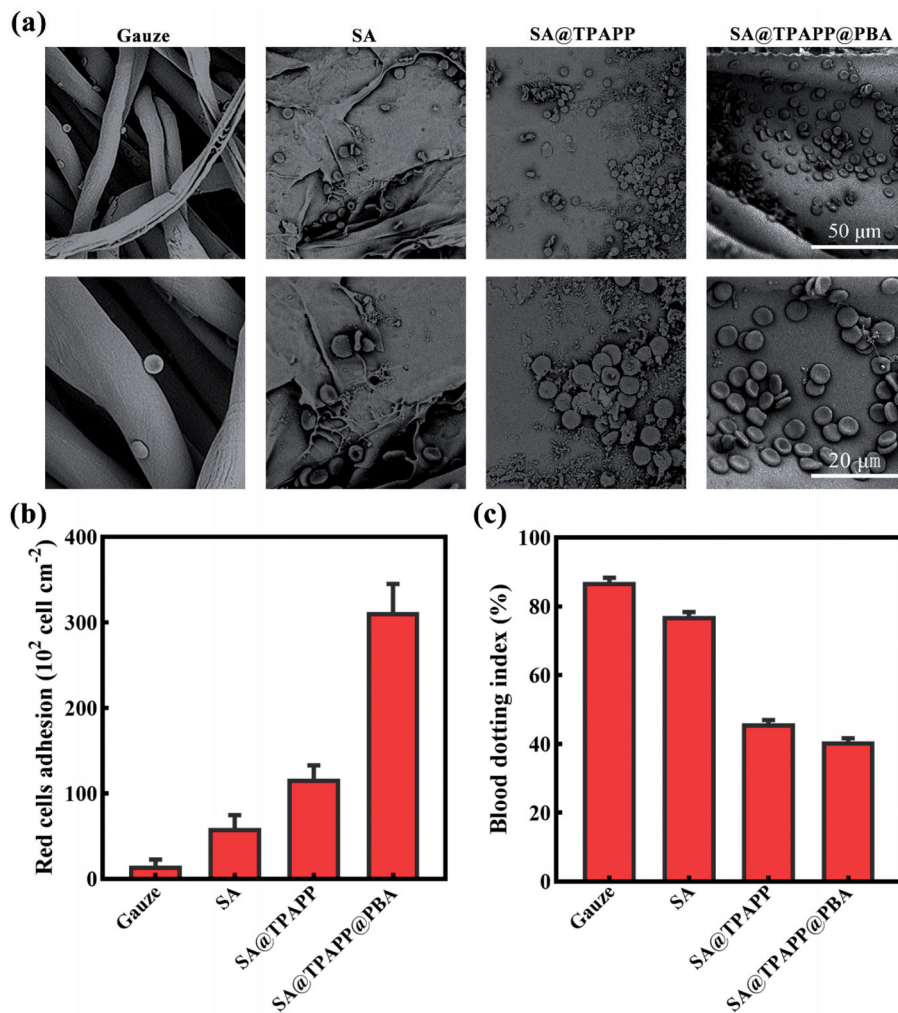

Figure 8. (a) SEM images of the blood red cells adhesion on gauze, SA, SA@TPAPP, and SA@TPAPP@PBA aerogels. (b) Related histogram of the red blood cells adhesion. (c) The blood dotting index.
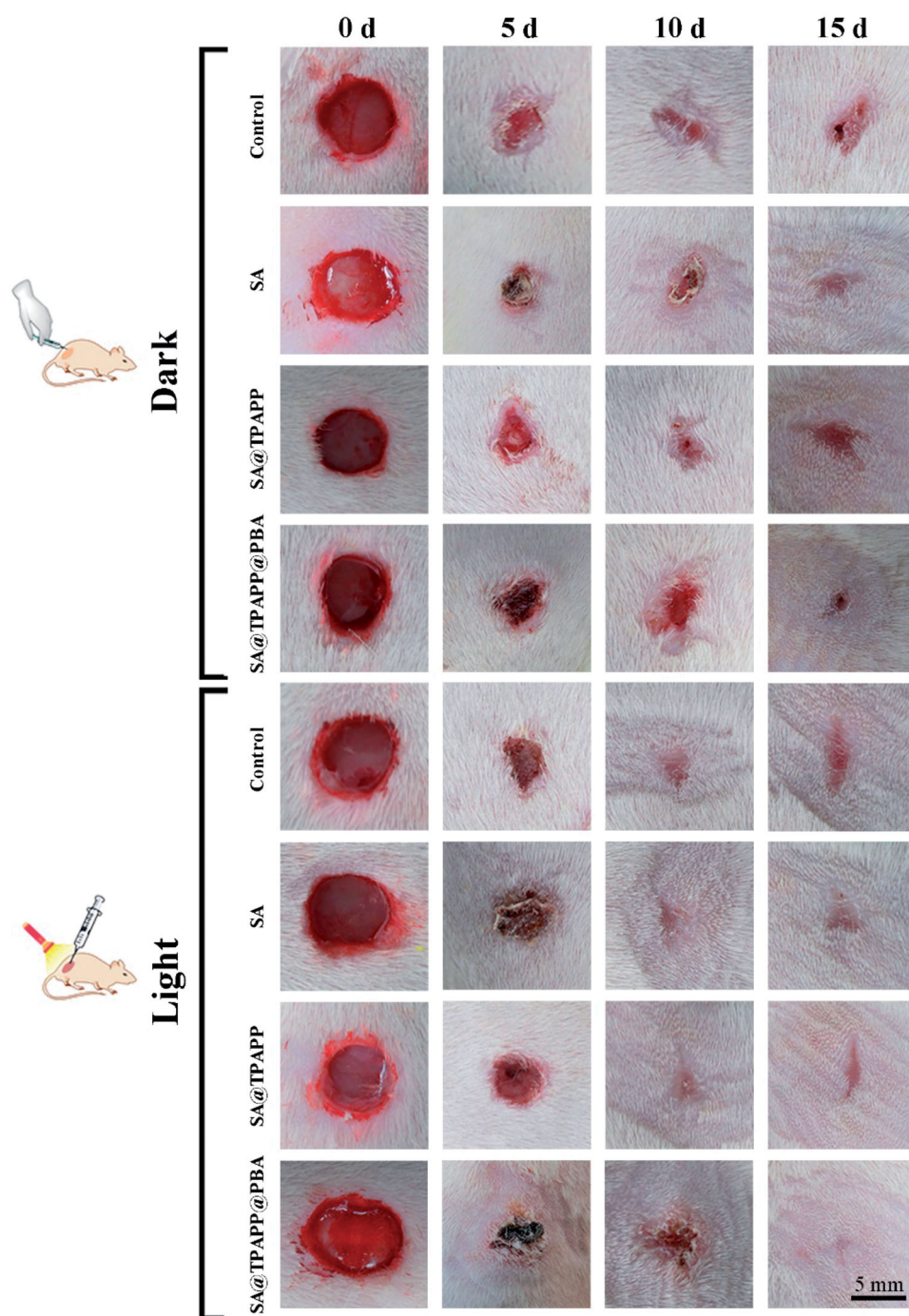
Figure 9. Photographs of the wound sites of rats after infection at 0, 7th, and 15th day.

(8) SA@TPAPP@PBA + Light (Figure 9). For comparison, SA and SA@TPAPP aerogels were dressed on the *S. aureus*-infected wound site in the absence and presence of a 660 nm laser illumination, respectively. As can be seen from Figures 9 and S4, the trauma still displayed about 20%, and serious bacterial infection took place in the unirradiated, SA + Light and SA@TPAPP + Light groups. In contrast, the area of scars in SA@TPAPP@PBA + Light group almost disappeared after 15 days due to the enhanced aPDT, which was in accordance with the *in vitro* antibacterial outcomes. After treatments, the mice were sacrificed and the skin of wound tissues was obtained for H&E staining (Figure 10). In the unirradiated groups and SA + Light group, large amounts of inflammatory cells exhibited in the entire wound site owning to *S. aureus* infection. In comparison, a decreased number of inflammatory cells were observed in SA@TPAPP + Light group due to aPDT. On the contrary, few inflammatory cells could be found in SA@TPAPP@PBA + Light group, proving dramatically reduced inflammation after enhanced aPDT, which further demonstrated its *in vivo* anti-inflammatory ability and great potential application in clinical trials.
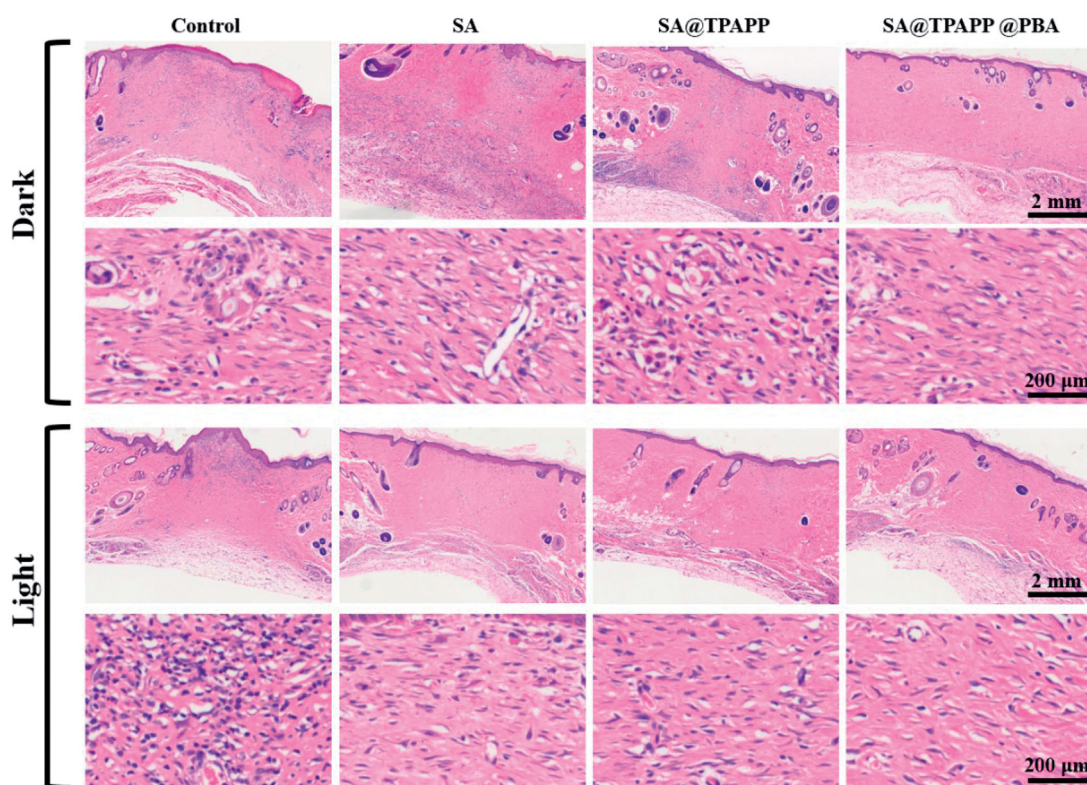
Figure 10. H&E staining of the wound section. Scale bar: 2 mm and 200 μm.

4. Conclusion

In conclusion, an antibiotic-free wound dressing, SA@TPAPP@PBA aerogel, has been developed for rapid hemostasis and enhanced aPDT against *S. aureus*. SA@TPAPP@PBA aerogel was produced by chemically conjugating photosensitizers TPAPP and PBA to the main chain of SA. Due to the PBA-mediated bacterial capture effect, *in vitro* antibacterial assays demonstrated that the therapeutic efficiency of SA@TPAPP@PBA aerogel against *S. aureus* was significantly enhanced under the irradiation of 660 nm laser. In addition, it possessed a high porosity, which was beneficial to blood exudate absorption and rapid hemostasis. Both *in vitro* and *in vivo* experiments proved that SA@TPAPP@PBA aerogel also demonstrated excellent biosafety, hemostatic, and anti-inflammatory capacities for pre-hospital care. Therefore, this multifunctional aerogel is a promising candidate for clinical trials as a wound dressing.

Disclosure statement

No potential conflict of interest was reported by the authors(s).

Funding

References

Aderibigbe BA, Buyana B. (2018). Alginate in wound dressings. Pharmaceutics 10:42.

Auzin A, Spits M, Tacconelli E, et al. (2021). What is the evidence base of used aggregated antibiotic resistance percentages to change empirical antibiotic treatment? A scoping review. Clin Microbiol Infect doi: 10.1016/j.cmi.2021.12.003

Bassetti S, Tschudin-Sutter S, Egli A, et al. (2022). Optimizing antibiotic therapies to reduce the risk of bacterial resistance. Eur J Intern Med. doi:10.1016/j.ejim.2022.01.029

Beyranvand S, Pourghobadi Z, Sattari S, et al. (2020). Boronic acid functionalized graphene platforms for diabetic wound healing. Carbon 158:327–36.

Cheng X, Li M, Wang H, et al. (2020). All-small-molecule dynamic covalent gels with antibacterial activity by boronate-tannic acid gelation. Chin Chem Lett 31:869–74.

Dharmaratne P, Sapugahawatte DN, Wang BY, et al. (2020). Contemporary approaches and future perspectives of antibacterial photodynamic therapy (aPDT) against methicillin-resistant *Staphylococcus aureus* (MRSA): a systematic review. Eur J Med Chem 200:112341.

Diniz IMA, Horta ID, Azevedo CS, et al. (2015). Antimicrobial photodynamic therapy: a promise candidate for caries lesions treatment. Photodiagn Photodyn Ther 12:511–8.

Dong R, Guo B. (2021). Smart wound dressings for wound healing. Nano Today 41:101290.

Feng YF, Coradi Tonon C, Ashraf S, et al. (2021). Photodynamic and antibiotic therapy in combination against bacterial infections: efficacy, determinants, mechanisms, and future perspectives. Adv Drug Deliv Rev 177:113941.

Galstyan A, Schiller R, Dobrindt U. (2017). Boronic acid functionalized photosensitizers: a strategy to target the surface of bacteria and implement active agents in polymer coatings. Angew Chem 129: 10498–502.

Gaston E, Fraser JF, Xu ZP, et al. (2018). Nano- and micro-materials in the treatment of internal bleeding and uncontrolled hemorrhage. Nanomedicine 14:507–19.

Guo XJ, Cao B, Wang CY, et al. (2020). In vivo photothermal inhibition of methicillin-resistant Staphylococcus aureus infection by in situ templated formulation of pathogen-targeting phototheranostics. Nanoscale 12:7651–9.

Hu C, Zhang F, Long L, et al. (2020). Dual-responsive injectable hydrogels encapsulating drug-loaded micelles for on-demand antimicrobial activity and accelerated wound healing. J Control Release 324:204–17.

Jia HR, Zhu YX, Chen Z, et al. (2017). Cholesterol-assisted bacterial cell surface engineering for photodynamic inactivation of Gram-positive and Gram-negative bacteria. ACS Appl Mater Interfaces 9:15943–51.

Kaya GG, Aznar E, Deveci H, et al. (2021). Aerogels as promising materials for antibacterial applications: a mini-review. Biomater Sci 9:7034–48.

Lai CKC, Ng RWY, Leung SSY, et al. (2021). Overcoming the rising incidence and evolving mechanisms of antibiotic resistance by novel drug delivery approaches – an overview. Adv Drug Deliv Rev 181:114078.

Lai-Cheong JE, McGrath JA. (2021). Structure and function of skin, hair and nails. Medicine 49:337–42.

Li J, Sun W, Yang Z, et al. (2020). Rational design of self-assembled cationic porphyrin-based nanoparticles for efficient photodynamic inactivation of bacteria. ACS Appl Mater Interfaces 12:54378–86.

Li J, Sun XJ, Zhang KC, et al. (2020a). Chitosan/diatom-biosilica aerogel with controlled porous structure for rapid hemostasis. Adv Healthcare Mater 9:2000951.

Li M, Zhang Z, Liang Y, et al. (2020b). Multifunctional tissue-adhesive cryogel wound dressing for rapid nonpressing surface hemorrhage and wound repair. ACS Appl Mater Interfaces 12:35856–72.

Liang Y, Li M, Yang Y, et al. (2022). pH/glucose dual responsive metformin release hydrogel dressings with adhesion and self-healing via dual-dynamic bonding for athletic diabetic foot wound healing. ACS Nano 16:3194–207.

Maleki A, He J, Bochani S, et al. (2021). Multifunctional photoactive hydrogels for wound healing acceleration. ACS Nano 15:18895–930.

McGrath JA, Uitto J. (2008). The Filaggrin Story: novel insights into skin-barrier function and disease. Trends Mol Med 14:20–7.

Meglio PD, Perera GK, Nestle FO. (2011). The multitasking organ: recent insights into skin immune function. Immunity 35:857–69.

Ren HH, Cui Y, Li AL, et al. (2018). Bioactive glass sol as a dual function additive for chitosan-alginate hybrid scaffold. Chin Chem Lett 29:395–8.

Stenflo J, Stenberg Y, Muranyi A. (2000). Calcium-binding EGF-like modules in coagulation proteinases: function of the calcium ion in module interactions. Biochim Biophys Acta 1477:51–63.

Sun YD, Zhu YX, Zhang X, et al. (2019). Role of cholesterol conjugation in the antibacterial photodynamic therapy of branched polyethylenimine-containing nanoagents. Langmuir 35:14324–31.

Toyoda T, Isobe K, Tsujino T, et al. (2018). Direct activation of platelets by addition of $CaCl_2$ leads coagulation of platelet-rich plasma. Int J Implant Dent 4:23.

Van der Vlies AJ, Morisaki M, Neng HI, et al. (2019). Framboidal nanoparticles containing a curcumin-phenylboronic acid complex with antiangiogenic and anticancer activities. Bioconjug Chem 30:861–70.

Varaprasad K, Jayaramudu T, Kanikireddy V, et al. (2020). Alginate-based composite materials for wound dressing application: a mini review. Carbohydr Polym 236:116025.

Wang H, Nie X, You W, et al. (2021). Tug-of-war between covalent binding and electrostatic interaction effectively killing E. coli without detectable resistance. ACS Appl Mater Interfaces 13:56838–49.

Wang H, Zhao BH, Dong WJ, et al. (2020). A dual-targeted platform based on graphene for synergistic chemo-photothermal therapy against multidrug-resistant Gram-negative bacteria and their biofilms. Chem Eng J 393:124595.

Wu S, Huang Y, Yan JC, et al. (2021). Bacterial outer membrane-coated mesoporous silica nanoparticles for targeted delivery of antibiotic rifampicin against Gram-negative bacterial infection in vivo. Adv Funct Mater 31:2103442.

Xian C, Gu Z, Liu G, et al. (2020). Whole wheat flour coating with antioxidant property accelerates tissue remodeling for enhanced wound healing. Chin Chem Lett 31:1612–5.

Xiao FF, Cao B, Wen LW, et al. (2020). Photosensitizer conjugate-functionalized poly (hexamethylene guanidine) for potentiated broad-spectrum bacterial inhibition and enhanced biocompatibility. Chin Chem Lett 31:2516–9.

Yao LT, Gao HC, Lin ZF, et al. (2022). A shape memory and antibacterial cryogel with rapid hemostasis for noncompressible hemorrhage and wound healing. Chem Eng J 428:131005.

Yao YX, Zhang AD, Yuan CS, et al. (2021). Recent trends on burn wound care: hydrogel dressings and scaffolds. Biomater Sci 9:4523–40.

Yu SM, Li GW, Liu R, et al. (2018). Dendritic Fe3O4@Poly(Dopamine)@PAMAM nanocomposite as controllable NO-releasing material: a synergistic photothermal and NO antibacterial study. Adv Funct Mater 28:1707440.

Zhang Y, Liu Y, Guo Z, et al. (2020). Chitosan-based bifunctional composite aerogel combining absorption and phototherapy for bacteria elimination. Carbohydr Polym 247:116739.

Zhao X, Pei D, Yang Y, et al. (2021). Green tea derivative driven smart hydrogels with desired functions for chronic diabetic wound treatment. Adv Funct Mater 31:2009442.

Zheng GD, Zheng JH, Xiao L, et al. (2021). Construction of a phenylboronic acid-functionalized nano-prodrug for pH-responsive emodin delivery and antibacterial activity. ACS Omega 6:8672–9.

Zheng L, Qi P, Zhang D. (2018). A simple, rapid and cost-effective colorimetric assay based on the 4-mercaptophenylboronic acid functionalized silver nanoparticles for bacteria monitoring. Sens Actuators B 260:983–9.

Zheng Y, Ma WP, Yang ZB, et al. (2022). An ultralong hydroxyapatite nanowire aerogel for rapid hemostasis and wound healing. Chem Eng J 430:132912.